Field Demonstration of Parallel Operation of Virtual Synchronous Controlled Grid-Forming Inverters and a Diesel Synchronous Generator in a Microgrid

QIANG LIN [1], **(Member, IEEE), HIROSHI UNO** [1], **KENICHIRO OGAWA** [1],
YASUHIRO KANEKIYO [1], **TETSU SHIJO** [1], **(Member, IEEE),**
JUNICHI ARAI [2], **(Life Senior Member, IEEE), TAKESHI MATSUDA** [3],
DAIKI YAMASHITA [4], **AND KENJI OTANI** [5]

[1] Toshiba Corporation, Kawasaki 212-8582, Japan
[2] Energy and Environment Technology Research Institute, Tokyo 169-0051, Japan
[3] Pacific Power Company Ltd., Tokyo 101-0054, Japan
[4] Pacific Consultants Company Ltd., Tokyo 101-8462, Japan
[5] National Institute of Advanced Industrial Science and Technology, Koriyama, Fukusima 963-0298, Japan

Corresponding author: Qiang Lin (qiang2.lin@toshiba.co.jp)

ABSTRACT With the growing shift toward renewable energy, attention focused on the disadvantages of current control inverter-based distributed generators, such as lack of grid-forming ability and inertia. To provide inertia support and grid-forming ability, virtual synchronous generators (VSGs) have been proposed. Various control methods related to VSGs have been reported, and various research challenges have been evaluated. However, only a few experimental demonstrations have been addressed. Recommended practices for VSGs were launched as IEEE Standard Project 2988 on March 25, 2021, with VSGs considered to be a new technology that is nearly ready to be put into practical use. Therefore, experimental demonstrations on a real-scale grid are important for establishing a technical standard for VSGs. In this study, a grid was built by simulating an actual microgrid on an approximately 1:1 power capacity scale. In the simulated grid, 125 kVA was provided by a diesel SG, five 20 kVA inverters with a battery energy system (BES) were used, and the power generation penetration of the inverter BES units achieved 44.4%. Six different penetration scenarios for operation of a grid forming inverter with BES (GFM-BES) and a grid following inverter with BES (GFL-BES) were evaluated comparatively. System inertia, and transient and steady state power sharing characteristics affected by different degrees of GFM-BES penetration under a sudden load change were demonstrated. Moreover, characteristics related to grid forming, synchronization, frequency regulation, and power regulation were demonstrated through field tests. The simulations and experiments also evaluated the inertia constant of a diesel SG, which is expected to be helpful for future simulations on this topic. The findings of this paper provide important instructions for engineers to model, design, and test distributed generators.

INDEX TERMS Distributed power generation, microgrid, diesel synchronous generator, virtual synchronous generator (VSG), parallel operation, grid-forming, inertia, experiment demonstration.

I. INTRODUCTION

Against a background of concerns about global climate change due to CO_2 emissions and fossil fuel resource depletion, distributed renewable energy power generation systems, such as solar power generation and wind power generation, have been developed in recent years [1]–[10]. Distributed renewable sources are connected to the grid via power inverters. Moreover, almost all of the grid-connected inverters are grid-following inverters (GFLs). GFLs need a

The associate editor coordinating the review of this manuscript and approving it for publication was Bin Zhou.

well-defined external voltage that allow their phase-locked loop (PLL) to follow the voltage, frequency, and phase in order to synchronize the inverter to the grid [1]. Although GFLs have the advantage of a faster response compared with conventional synchronous generators (SGs), two drawbacks have been noted for GFLs. First, they do not have an inertial ability and cannot form a grid, and this has limited the penetration of GFLs in power systems up to now. As the penetration of GFLs increases, this will reduce the inertial ability and synchronization force of the entire system. It is difficult for a low proportion of SGs to maintain the system frequency, and the stability of the system will be reduced. Second, GFLs cannot work in a stand-alone mode. Because the control method for GFLs needs a PLL to synchronize the inverter to the grid, GFLs are not able to black start.

To maintain a healthy grid, a variety of grid-forming methods have been developed. Inverters with grid-forming controllers are called grid-forming inverters (GFMs). GFMs allow GFLs, other GFMs, and SGs to coexist in the same system [2]. GFMs can be categorized as droop control inverters [3]–[6], virtual synchronous inverters [7]–[30], and virtual oscillator inverters [31].

Droop control inverters can imitate the steady-state characteristics of SGs, as originally proposed in [3]. These inverters introduce a linear trade-off between active-power frequency and reactive-power voltage [4]–[6]. When applied to microgrid systems, droop control inverters usually contribute to the primary control, in which the steady-state power sharing of parallel inverters depends on the capacity of the inverters and the droop slope rate.

Droop control inverters can improve the power sharing ability and stability of a system. However, systems with droop control inverters still do not have inertial support, and transient changes are not satisfactorily controlled. To enhance the inertial ability of power systems, virtual synchronous machines (VSMs) [7]–[10], synchronverters [11]–[14], and virtual synchronous generators (VSGs) [15]–[22] have been proposed. Specifically, these methods imitate mainly the body model of an SG, active-power and frequency regulation, and the characteristics of reactive-power voltage regulation. Therefore, these methods allow inverters to be operated as traditional SGs in terms of the operating mechanism and external characteristics. Current-controlled VSMs were first proposed in [7], which simulated mainly the swing equation of the SG by external characteristics and did not simulate the voltage regulation characteristics of an SG. Furthermore, technology in [8]–[10] can better reflect the whole operating characteristics of SGs.

However, current-controlled VSMs are equivalent to a current source, and they cannot easily provide voltage and frequency support for the system. To make up for the shortcomings of current-controlled VSMs, voltage-controlled virtual synchronous inverter technology has been proposed [11]–[28]. Some proposed synchronverters incorporate the dynamic model of the AC side of the inverter, and at the same time consider the electromechanical and electromagnetic transient characteristics of the SG [11]–[13]. Such synchronverters realize the physical and mathematical model equivalent of the SG very well. They can also realize the self-synchronization operation of the inverters without a PLL [14]. However, the second-order model used in synchronverters is complex, and a huge number of parameter settings are needed. A VSG [15]–[22] used as a first-order model that is based mainly on the mechanical transient characteristics of the SG has been reported. It improves the stability of the system frequency by imitating the inertia of the rotor and the frequency control characteristics of the SG. In terms of voltage control, the reactive power and voltage relationship is considered to stabilize mainly the output voltage. The power controller and voltage frequency controller give the VSG the dual functions of power control and frequency modulation. Although the principle of the VSG is the same, the basic control method is not unique. Various control methods related to VSGs have been reported, including frequency and voltage control [15]–[20], system protection [21]–[24], fault ride-through and system recovery [25]–[26], and modeling and simulation [27]–[28].

Various research challenges for VSGs have been discussed in the literature cited above. However, only a few experimental demonstrations have been reported. The IEEE Standard Project 2988 for VSGs was launched on March 25, 2021, and it is considered to be a new technology that is nearly ready for practical use. Therefore, experimental demonstrations on a real-scale grid are important for establishing technical standards for VSGs. A small-scale microgrid field demonstration with five VSGs was implemented in [14]. The autonomous operation of a home grid to achieve tight voltage and frequency regulation was demonstrated without relying on a communication network. However, the home grid did not contain an actual SG, the parallel operation characteristics of VSGs and SGs were not clarified, and control of transient phenomena were not discussed. Reference [29] discussed the parallel operation characteristics of VSGs and SGs, and [27] discussed the transient characteristics of VSGs in parallel with SGs. However, the SGs in [27] and [29] were motor generators, which are usually used for experiments in the laboratory. The characteristics of VSGs with a real SG are not clear. Referene [30] characterized a real stand-alone gas-engine generator using a VSG and energy storage system, but in a small-scale system.

Motivated by the above issues, the following novelties are presented to contribute to the body of knowledge.

1) We proposed a large-scale microgrid structure for operational evaluation. The microgrid consists of VSGs and a real diesel SG, which was constructed based on a real local microgrid. Almost the same power generation capacity and load change as a real local microgrid are used for experiments and evaluation. Moreover, the proposed microgrid increased the penetration ratio of inverters to 44.4%, which can offer a new style of distributed power generation system.

2) Because the rotor inertia constant of a diesel SG is not clearly established, we inferred the approximate inertia constant of the diesel SG from the experimental results in SG stand-alone mode. The SG model was constructed and the inferred inertia constant is then compared with the fitted inertia constant in the simulation for verification. This is expected to be helpful for simulations by other researchers on this topic.

3) A sudden-load-change demonstration experiment was implemented, and the characteristics of grid forming, synchronization, frequency regulation, and power sharing were demonstrated through field tests.

4) We proposed an evaluation scheme. The inverter with battery energy system (inverter-BES) could operate in grid forming inverter with BES (GFM-BES) mode or grid following inverter with BES (GFL-BES) mode. Under the parallel operation of the five 20-kVA inverter-BES and the 125-kVA SG, six different combinations of GFM-BES and GFL-BES operation were evaluated comparatively. Different cases demonstrated that the system inertia was improved by increasing the penetration ratio of GFM-BES.

5) Autonomous operation of the simulated grid to achieve frequency and power regulation were demonstrated without relying on a communication network.

6) We verify the inertial frequency step response by evaluating the frequency nadir and rate of change of frequency (RoCoF) of the experimental results, which demonstrate the actual inertial characteristic in the microgrid contained a diesel SG.

7) The actual transient and steady-state power sharing characteristics in the microgrid under different penetration ratios of GFM-BES are analyzed and demonstrated.

8) There were some findings learned from the actual tests that were not predicated by the simulations. Because the inertia constant of the 125-kVA SG is very small, a large load change may cause the inverters to shut down for protection in low GFM-BES penetration ratio cases. The step response delay of the diesel SG is not constant because of its actual mechanical characteristics, and the delay varies between different load changes. The high quality BES can recharge very quickly to provide inertial energy

The remainder of this paper is organized as follows. The architecture and control scheme of GFM-BES are introduced in Section II. The simulated microgrid used for the demonstration is shown in Section III. In Section IV, the inertia of the diesel SG used in the demonstration experiment is tested, and the inertia constant is inferred by experimental results and simulation tuning. In Section V, parallel demonstration experiments of SG and inverter-BES are implemented. System inertia, and transient and steady state power sharing are discussed for different SSI-BES penetration ratios. Finally, conclusions are made in Section VI.
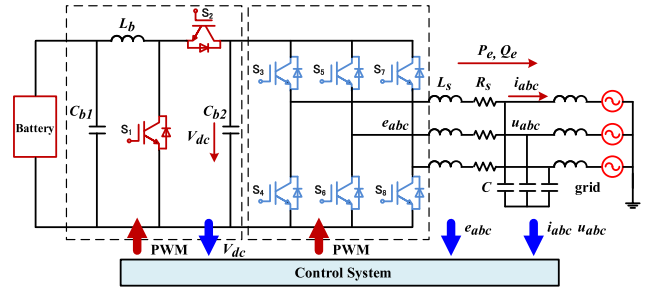

FIGURE 1. Basic topology of GFM-BES.

II. PRINCIPLE OF VOLTAGE-CONTROLLED GFM-BES

A. BASIC TOPOLOGY OF GFM-BES

In this paper, the GFM-BES consists of a 15-kWh lithium-ion battery (Toshiba SCiB^{TM}), a DC/DC converter, and a three-phase 202-V/20-kVA inverter. These were installed in a $1,200 \times 530 \times 1,715$ mm frame. The main circuit of the GFM-BES is shown in Figure 1, where u_{abc}, e_{abc}, and i_{abc} are the GFM-BES three-phase output voltage, induced electromotive force, and three-phase output current, respectively; R_s and L_s are the equivalent stator resistors and equivalent synchronous inductors, respectively; and P_e and Q_e are the real power and reactive power output by the GFM-BES, respectively.

The control system consists mainly of the main body model and a control algorithm. The main body model simulates the mechanical motion characteristics of the synchronous generator from the operating mechanism, and the control algorithm simulates the external characteristics of the SG, such as the active power-frequency adjustment characteristics and the reactive power-voltage adjustment characteristics.

B. CONTROL SCHEME OF GFM-BES

Figure 2 shows a schematic block diagram of the GFM-BES control algorithm [21]. The inertial force and braking characteristics of the rotor are simulated based on the equation of motion of the SG rotor in (1). The active power and frequency control operation by the droop governor can be represented by (2), where J is the inertia moment, ω_{mea} is the system angular frequency, ω_{ref} is the command value of system angular frequency, T_m is the mechanical torque, T_e is the electrical torque, T_d is the braking torque, P_{ref} is the command value of active power, P_{mea} is the output active power, k_{droop} is the droop rate of the governor, and ΔP is the load sudden change.

$$T_m - T_e - T_d = \frac{P_{ref} + P_{droop} - P_{mea}}{\omega} = J\frac{d\omega_{mea}}{dt} \quad (1)$$

$$\Delta P = (\omega_{ref} - \omega_{mea})\frac{1}{k_{droop}} \quad (2)$$

The unit inertia coefficient M can be calculated from (3) and (4), where M_0 is the inertia coefficient and P_{base} is the base power for per unit (pu) calculation.

$$M_0 = J\omega_{ref}^2 \quad (3)$$

$$M = \frac{M_0}{P_{\text{base}}} \qquad (4)$$

The GFM-BES receives the values of the frequency command, active power command, voltage command, and invalid power command from the host control system, such as an energy management system (EMS). The inertia imitation unit consists of a first-order delay $1/(1 + 8\,s)$ and phase compensation $(1 + 0.16\,s)/(1 + 0.04\,s)$ for open-loop phase margin, assuming a unit inertia coefficient of 8 s as a general synchronous generator. The output phase signal δ is then calculated through integration of the command angular frequency and deviation angular frequency. When an GFM-BES unit is started, the phase of the system-side voltage is detected and that phase is set as the initial value at startup. This eliminates the difference between the voltage phase generated by the inverter at startup and the phase on the system side, enabling synchronous startup without transient phenomena. The three-phase voltage signals V_a, V_b, and V_c are created from the phase signal δ and the voltage amplitude signal E given by the voltage control unit. The three-phase voltage signal is transferred to the pulse width modulation (PWM) block, and the on/off pulse of each arm of the inverter is determined.

As with the SG, droop control is added and is performed so as to contribute to maintaining the frequency of the system. In voltage control, the voltage at the point where the inverter is connected with the system side is controlled to be constant. Reactive power control is implemented in the same way as in the SG. This GFM-BES operates in parallel with the SG. During operation, neither the PLL that detects the phase of the voltage on the system side nor the current control is used for the inverter. Each GFM-BES unit generates a three-phase voltage and operates in synchronization with other power sources, such as the SG. Because the GFM-BES is designed to imitate an SG, it continues to operate until its own device protection is activated. Therefore, the fault ride through (FRT) function is not implemented. In addition, GFM-BES has the same characteristics as a generator and is treated with the same considerations, so the independent operation detection function is not implemented.

III. DESCRIPTION OF THE IMITATED MICROGRID
A. MICROGRID CHARACTERISTICS
The inverters had two control modes, GFL-BES mode and GFM-BES mode. All the GFM-BES units are equipped with a self-synchronized droop controller with many advanced functions, including black-start and grid-forming capabilities, self-synchronization without a PLL, voltage and frequency regulation, and power-sharing control. The purpose of the developed GFM-BES was to achieve stable operation in off-grid locations, microgrids, or islands with over 70% penetration rate of renewable energy sources in the future, and contribute to CO_2 emission reduction. In particular, in conventional research and development, installing a large battery storage system in one place is efficient for large-scale systems such as power transmission and distribution systems
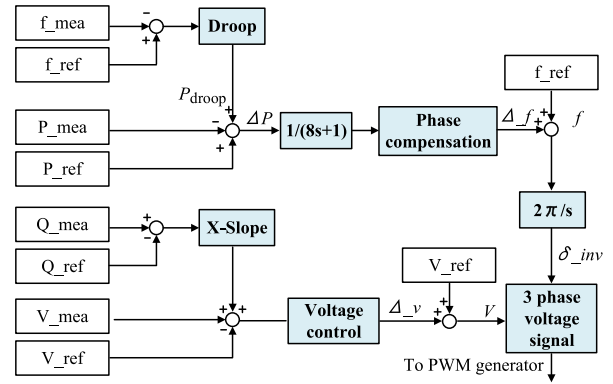

FIGURE 2. Block diagram of GFM-BES control algorithm.

where power demand and power supply configurations do not change easily. However, in islands and microgrids, it is considered difficult to apply a large-scale system from the point of view of ensuring the flexibility of system construction. In contrast, the approach of installing a battery storage system in a small and distributed manner is suitable for flexibly changing the system configuration according to changes in the supply and demand.

Therefore, GFM-BES is thought to be suitable for application in relatively small-scale grids, such as new regional electric power systems and off-grid locations. The battery packs store energy when the load demand is less than the generation capacity, and release energy when the load demand is greater than the capacity.

The microgrid used for the demonstration experiment was built based on a real microgrid in Mutsuzawa, Japan. The semi-microgrid in Mutsuzawa consists of two SG 80-kVA units, a 20-kW PCS-PV system, and a load (20 home units). Based on the real load fluctuation data in Mutsuzawa shown in Figure 3, a nearly 50-kW-scale load changes occur over a short time. The simulated microgrid was built with the microgrid architecture and simulated using a diesel SG and GFM-BES units at approximately 1:1 power capacity scale with Mutsuzawa, and was operated under the same load changes. In the simulated grid, inverter-BES units are used instead of part of the SG capacity, and the inverter-BES
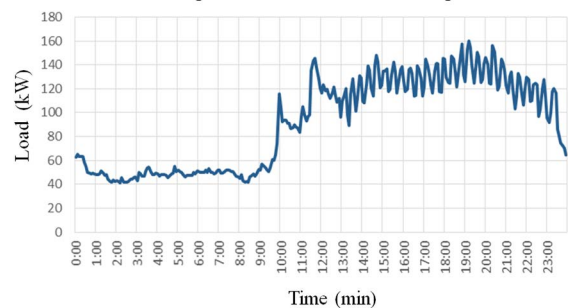

FIGURE 3. Real load change data of Mutsuzawa, Japan, over 23 min.

units achieved a power generation penetration of 44.4%. The configuration of the simulated microgrid is shown in Figure 4. In this study, an experimental demonstration based on the real power capacity scale model was implemented.
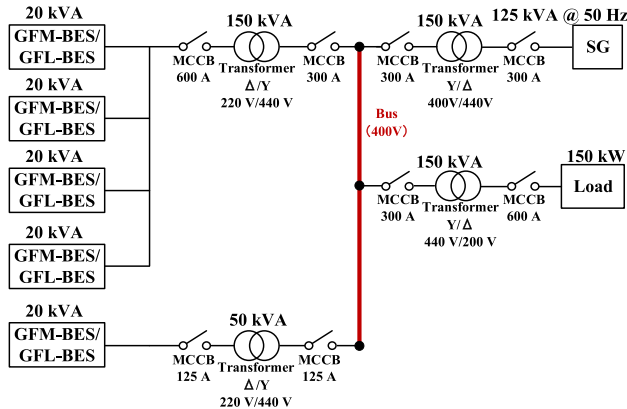

FIGURE 4. Configuration of the simulated microgrid (MCCB = molded-case circuit breaker).

B. CONFIGURATION OF THE IMITATED MICROGRID

Figure 4 shows the microgrid system comprising a 125-kVA SG, which is the main power generator of the microgrid, and five 20-kVA inverter-BES units. The voltages of the inverters are set to 202 V for the voltage drop of the transmission lines. Because proof of concept (PoC) safety management is difficult if the power grid is set to 6.6 kV, the power grid was set to 400 V. Considering the flow ability of the transformer, a Y connection node was used for the bus side. The neutral point of the Y connection side floated. Three 50-kW three-phase devices were connected in parallel as the load. To confirm the effect of the transformer, one of the five inverter-BES units was connected under a 50-kVA transformer. Figure 5 shows the 125-kVA diesel generator, for which the terminal voltage was set to 440 V and the operation frequency was 50 Hz. Figure 6 shows the demonstration environment, which was housed in a shielded room. Field operation of the microgrid was performed to demonstrate the operation of the system: (1) Evaluation of the inertia constant of the diesel SG by

FIGURE 5. 125-kVA diesel synchronous generator.

FIGURE 6. Demonstration environment in a shield room.

simulation and experiment; (2) Multiple GFM-BES units in parallel with diesel SG and GFL-BES to respond automatically to load fluctuations within a few seconds without relying on a communication network; (3) Many advanced functions, namely, grid forming, synchronization, frequency regulation, and power sharing; (4) Confirmation of the inertial effect on frequency fluctuations according to sudden load changes under the cases of different ratio of GFM-BES penetration; (5) Confirmation of the effect of the impedance of the transformer; (6) Confirmation of power sharing in transient and steady states.

C. FREQUENCY MEASUREMENT

The grid frequency was calculated by counting the number of zero crossings of the grid voltage. A moving average method was then implemented for the frequency average calculation to reduce error. It is important to select an appropriate sampling frequency for the measurement instruments and select an appropriate interval time for the moving average method. In this study, a power scope with a sampling frequency of 50 k/s is selected for grid voltage measurement. Because the commanded grid frequency is 50 Hz, the interval range for the moving average calculation was set to 100 points. This means that the frequency is refreshed every 0.002 s after the moving average calculation. Because the grid frequency changes every 0.02 s, the frequency calculation is thought to be accurate.

IV. GFM-BES AND DIESEL SG IN STAND-ALONE MODE

Because demonstration experiments in the field of power systems are expensive and difficult to implement for many researchers, simulation is an important research method, and parameters that closely approximate real equipment are very important for accurate modeling and simulations. For example, according to the standard system model of the Institute of Electrical Engineers of Japan, the rotor inertia constant of a large-capacity thermal power generator is between 7 s and 10 s. It is convenient to use this value for a large-scale grid simulation. However, the rotor inertia constant of the small-capacity power generators used for small-scale

TABLE 1. Parameters of GFM-BES and diesel SG.

Parameter	Value	Parameter	Value
$V_{\text{base\_GFM}}$	200 V	M_{GFM}	8.0 s
$S_{\text{base\_GFM}}$	20 kVA	D_{GFM}	1.0
$f_{\text{base\_GFM}}$	50 Hz	Droop gain (GFM-BES)	-4%
L_s	0.05 pu.	Xslope gain	-4%
Phase compensation	(1+0.16s)/(1+0.04s)	Voltage control	20/s
$V_{\text{base\_SG}}$	400 V	$S_{\text{base\_SG}}$	125 kVA
$f_{\text{base\_SG}}$	50 Hz	Droop gain (SG)	-4%
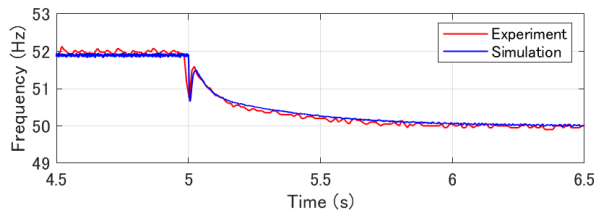
FIGURE 7. Frequency regulation of GFM-BES operating on stand-alone mode.

grids, such as microgrids, has not been clearly established. This section describes how the rotor inertia constant of the 125-kVA diesel SGs used in small-scale microgrids was surveyed by calculating from the experimental results. The calculated results were compared with simulation results.

A. GFM-BES IN STAND-ALONE MODE
First, simulation of the GFM-BES stand-alone mode was implemented to compare the result with the experimental result. Parameters for the GFM-BES are shown in Table 1. The active power command value for the GFM-BES was 20 kW, and the load change was 20 kW. As shown in Figure 7, the slopes of the frequency decrease in the simulation result and experimental result are almost the same. This confirms that the GFM-BES operated as designed.

B. SG IN STAND-ALONE MODE
The parameters of the SG as taken from the nameplate are shown in Table 1. Because the rotor inertia constant of diesel SGs has not been clearly established, the approximate inertia constant of the diesel SG is inferred from the experimental results. The inferred inertia constant is then compared with the fitted inertia constant in the simulation.

The inertia constant can be calculated based on the swing equation of the SG rotor as shown in (5) where M is the unit inertia constant, ω_{mea} is the system angular frequency, T_m is the mechanical torque, T_e is the electrical torque, T_d is the braking torque, P_m is the mechanical power of SG, P_{mea} is the electrical output of the active power, and P_d is the braking power.

$$T_m - T_e - T_d = \frac{P_m - P_{\text{mea}} - P_d}{\omega_{\text{mea}}} = M \frac{d\omega_{\text{mea}}}{dt} \quad (5)$$

Equation (6) is defined for the case of a sudden load change ΔP occurring. The braking power P_d is ignored for simplicity of calculation.

$$\Delta P = P_m - P_{\text{mea}} = M \omega_{\text{mea}} \frac{d\omega_{\text{mea}}}{dt} \quad (6)$$

Three cases of sudden load change experiments, for changes of 20 kW, 30 kW, and 50 kW are implemented for determining the inertia constant. The frequency regulation of the SG operating in stand-alone mode is shown in Figure 8 for the three cases. Based on (6), the change in frequency over 0.1 s was used for the calculation. The instantaneous frequency and frequency deviation and the calculated inertia constant of the three cases are summarized in Table 2. Note that all of the parameters in the calculation use the pu value. The inertia constant of the diesel SG is approximately 1.5 s.
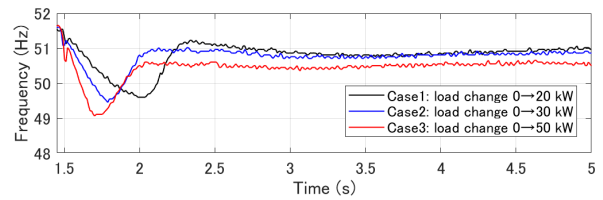

FIGURE 8. Frequency regulation of SG operating on stand-alone mode in three cases load change experiment.

TABLE 2. Inertia calculation of SG from experimental results.

Metric	Case 1	Case 2	Case 3
Load change (kW)	20	30	50
instantaneous frequency in experiment (Hz)	50.76	50.36	49.64
Frequency deviation in experiment (Hz)	0.52	0.72	1.26
Calculated from experiment M (s)	1.51	1.65	1.59

The SG model shown in Figure 9 is studied in the simulation. The model was also built based on the swing equation of the SG rotor. The delay of the power regulation is emulated by T_{sg}. The SG parameters in the simulation are summarized in Table 3. Like the experiment, three cases of
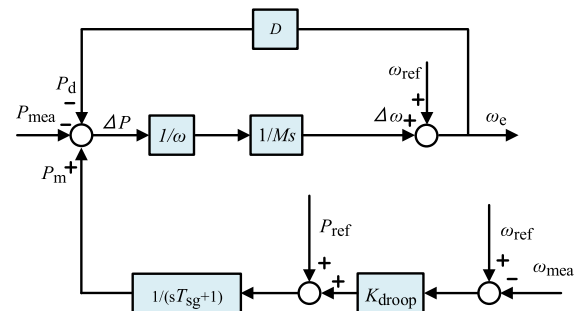

FIGURE 9. Block diagram of SG control algorithm used in simulation.

TABLE 3. Parameters of SG in simulation.

Parameter	Value	Parameter	Value
$V_{base\ SG}$	400 V	X_d'	0.3 pu
$S_{base\ SG}$	125 kVA	X_d''	0.23 pu.
$f_{base\ SG}$	50 Hz	X_q	1.65 pu.
$M_{sg\ fitted}$	1.12 s	X_q'	0.25 pu
$M_{sg\ default}$	0.34 s	X_q''	0.15 pu.
X_d	1.81 pu	T_{SG}	0.3 s

sudden load changes of 20 kW, 30 kW, and 50 kW were implemented to evaluate the inertia constant. A fitted inertia constant of 1.12 s was obtained by tuning the parameter of M in Figure 9. Because the rotor inertia constant of diesel SGs has not been clearly established, the parameters of the SG model in MATLAB were used for reference. As shown in Table 4, 0.34 s was assumed for the default inertia constant of the 125-kVA diesel SG. When the load change is 50 kW, the simulation and experimental results of the SG in stand-alone mode are compared. Comparisons of SG with the default inertia constant 0.34 s, and the fitted inertia constant 1.12 s, and the experiment results are shown in Figure 10. With the default value, the frequency slope of the simulation is smaller than that of the experimental results. With a fitted inertia constant of 1.12 s, the frequency slope of the simulation matches the experiment very well.
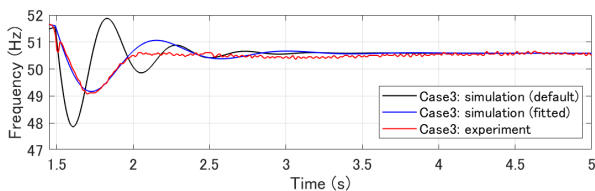

FIGURE 10. Frequency regulation of SG operating on stand-alone mode in three cases load change experiment.

TABLE 4. SG parameters in MATLAB model.

Case	Frequency	Capacity	Pole Pairs	M
1		85 kVA	4	0.2072 s
2	50 Hz	250 kVA	4	0.3506 s
3		670 kVA	4	0.3694 s
4	60 Hz	100 kVA	4	0.2536 s
5		300 kVA	4	0.3972 s

The difference in the inertia constant of the SG between the value calculated from the experimental results and the value obtained by fitting to the simulation is probably due to differences between the calculation and the real mechanical characteristics of the actual diesel SG. This paper discusses only the effect of the rotor inertia constant, and studying the effect of other parameters is planned as future work. The inertial constant of the 125-kVA diesel SG is considered to be around 1.12 s.

The frequency regulation of an SG operating in stand-alone mode in the simulation is shown in Figure 11 for the three cases. Compared with the experimental results in Figure 8, it can be seen that the time to reach the minimum frequency is the same in the simulation but different in the experiment. The time to reach the minimum is affected mainly by T_{SG}, which is the power regulation delay. Although it is a constant value in the simulation and the delay in a real diesel SG is controlled by an electric governor, the load change response speed is also affected by the value of the load change. This is one lesson learned from the demonstration experiment.
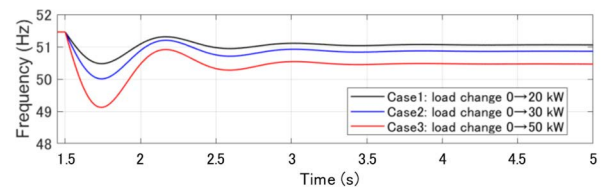

FIGURE 11. Frequency regulation of SG operating on stand-alone mode in three cases load change simulation.

V. GFM-BES IN PARALLEL WITH GFL-BES AND A DIESEL SG

The developed GFM-BES units can be switched to GFL-BES mode, which is a normal current control inverter mode, by setting the control software. Under the parallel operation of five 20-kVA inverter-BES units and the 125-kVA SG, the penetration ratio of GFM-BES and GFL-BES was changed in six cases. The response to load changes of the SG, GFM-BES, and GFL-BES were compared for system inertia evaluation in a sudden load change experiment.

A. RESULTS FROM FIELD OPERATIONS

The parameters of the GFM-BES units and diesel SG are shown in Table 1. The experimental conditions are shown in Table 5. The initial load was 72 kW. All of the active power reference values of the inverters were set to 6.4 kW, with the remaining 40 kW shared by the SG. The rotor speed of the SG was adjusted by operating the operation panel of the SG until a grid frequency of 50 Hz was achieved. At this moment, the active power command value of the SG was 40 kW theoretically. This is considered the initial state.

TABLE 5. Experimental conditions.

Case #	Numbers of Inverters		GFM-BES penetration (power capacity of GFM-BESs / power capacity of total system) (%)	Load change (kW)
	GFM-BES	GFL-BES		
Case 1	0	5	0	72 to 120
Case 2	1	4	8.8	72 to 120
Case 3	2	3	17.7	72 to 120
Case 4	3	2	26.6	72 to 120
Case 5	4	1	35.5	72 to 120
Case 6	5	0	44.4	72 to 120

Because the inertial constant of the GFM-BES is 8 s, 10 s of data were taken by power scope for each experiment.

In case 1, five GFL-BES units and one SG were operated in parallel. The load changed from 72 kW to 120 kW at $t = 1.5$ s, and the power sharing and frequency change are shown in Figure 12. Because the GFL-BES units do not have inertia, it was found that even if the load fluctuated at $t = 1.5$ s, the GFL-BES output followed the reference value of 6.4 kW without sharing the load. The load sharing of the SG is 90 kW, which is equivalent to 0.4 pu of power generation capacity. As the load increases, the grid frequency gradually drops due to the inertia of the SG, and finally has a significant transient drop to 47.6 Hz. It can be concluded that the inertia of the diesel SG is very small. After this, the synchronous force of the SG accelerates the rotor, and the grid frequency returns to 49.47 Hz due to the frequency drooping characteristics in steady state.
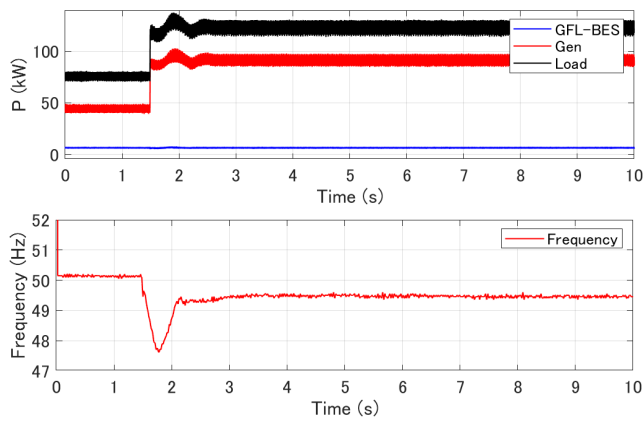
FIGURE 12. Case 1: Power sharing and grid frequency change for five GFL-BES units, zero GFM-BES units, and one SG.

The power sharing and frequency change in case 2 are shown in Figure 13. The active power reference value of the GFM-BES is 6.4 kW. Because the grid frequency is 50 Hz until $t = 1.5$ s, the actual output of the GFM-BES units is also 6.4 kW, as commanded. The output of the GFL-BES units still follows the reference value of 6.4 kW without sharing the load change. After the load change at $t = 1.5$ s, the load is shared by one GFM-BES unit and the SG together. At the moment of load fluctuation, the GFM-BES and SG share the load fluctuation at the same time by the mutual synchronization force. After this, the output of the GFM-BES gradually increases, and the output of the SG gradually decreases. However, due to the low inertia of the diesel SG, the frequency deviation is very large during transients. Due to the droop control and inertia of the GFM-BES, the output of the GFM-BES keeps increasing to regulate the frequency deviation. Finally, it reaches the overload protection limit and shuts down the inverter. Although the load change of 48 kW, which is equivalent to 0.213 pu of the power generation capacity, is not large, it should be noted that the inertia of the diesel SG is too low and may cause GFM-BES shutdown when GFM-BES units operate with a diesel SG.
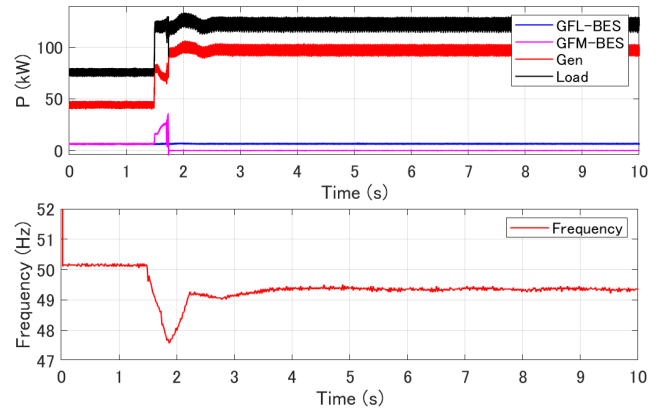

FIGURE 13. Case 2: Power sharing and grid frequency change for four GFL-BES units, one GFM-BES unit, and one SG.

The power sharing and frequency change in case 3, where two GFM-BES units are active, are shown in Figure 14. When the frequency was 50 Hz before $t = 1.5$ s, the droop control of the GFM-BES did not operate and the GFM-BES output before $t = 1.5$ s is the same as the commanded value of 6.4 kW. The GFL-BES operated in the same way as discussed above. When the load suddenly changed at $t = 1.5$ s, the GFM-BES and SG start to share the load change due to the mutual synchronous force. The GFM-BES output then increases gradually, and the SG output decreases gradually until both reach a steady state. Load sharing of SG and inverters in the steady state can be calculated based on (7) and (8), where ΔP is the total load change, P_{ni} is the rated power of each power generation device, ΔP_i is the power sharing of each power generation device, K_{droopi} is the droop rate of each device. f_n is the based frequency, and Δf is the frequency deviation in the steady state.

$$\Delta f \, [\text{pu}] = -K_{\text{droop1}} \frac{\Delta P_1}{P_{n1}} = \ldots - K_{\text{droopn}} \frac{\Delta P_n}{P_{nn}} \quad (7)$$

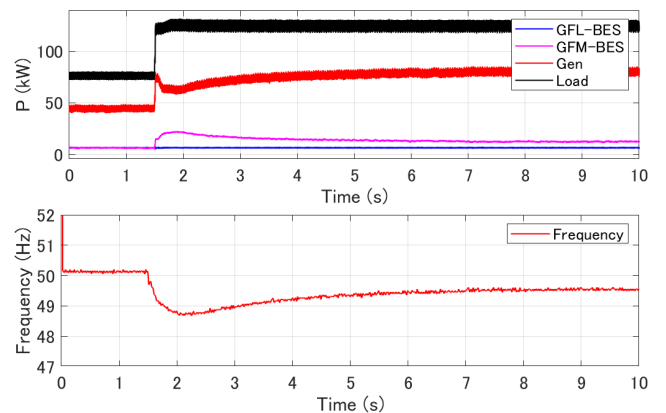$$\Delta P = \Delta P_1 + \Delta P_2 + \ldots \Delta P_n \quad (8)$$

FIGURE 14. Case 3: Power sharing and grid frequency change for three GFL-BES units, two GFM-BES units, and one SG.
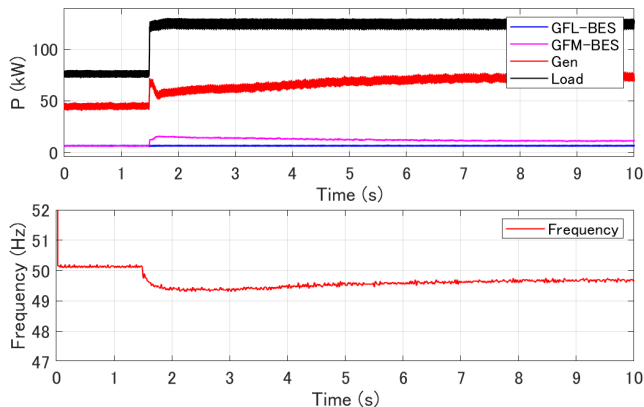
FIGURE 15. Case 4: Power sharing and grid frequency change for two GFL-BES units, three GFM-BES units, and one SG.

FIGURE 16. Case 5: Power sharing and grid frequency change for one GFL-BES unit, four GFM-BES units, and one SG.

Eliminate Δf from (7) and (8), so that

$$\Delta P_i = \left(\frac{\frac{P_{ni}}{K_{\text{droopi}}}}{\sum_{j=1}^{n} \frac{P_{nj}}{K_{\text{droopj}}}} \right) \Delta P \qquad (9)$$

Because the droop gain of the GFM-BES and SG units is the same as shown in Table 1, the load sharing in the steady state is proportionally shared with the rated power of each power generation device. In the steady state, the load sharing calculated from (9) is 12.2 kW for the GFM-BES and 76.3 kW for the generator, which matches the test results in Figure 14. It was confirmed that the GFM-BES units could share the load power autonomously. When the load suddenly changed at $t = 1.5$ s, the frequency gradually decreased to 48.68 Hz due to the inertia of the power generation device, the frequency increased due to the synchronization force of the power generation device, and the system frequency returned to 49.53 Hz due to the frequency drooping characteristic. By increasing the penetration ratio of GFM-BES in the system, the inertia of the system could be increased and the frequency deviation during transients could be suppressed.

Three GFM-BES units were implemented in case 4. The power sharing and frequency regulation are shown in Figure 15. In the case where the load changed to 48 kW, the maximum transient power sharing of each GFM-BES unit was 17.7 kW, and the maximum frequency deviation was 0.93 Hz. Increasing the penetration ratio of GFM-BES significantly improved the stability of the system. The power sharing and frequency change in cases 5 and 6 are shown in Figures 16 and 17, respectively. The number of GFM-BES units in the system increased from four to five. The frequency nadir reduction effect by GFM-BES due to inertia imitated control was further confirmed.

B. EFFECT OF TRANSFORMER IMPEDANCE

The active power output of each GFM-BES unit when all five units were operated in parallel is shown in Figure 18. All five GFM-BES units have the same characteristics. Four
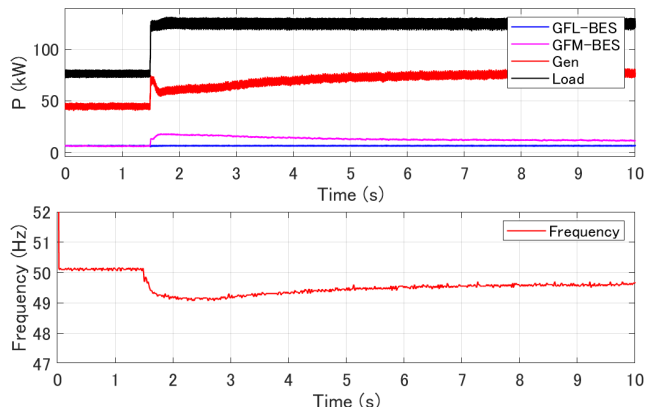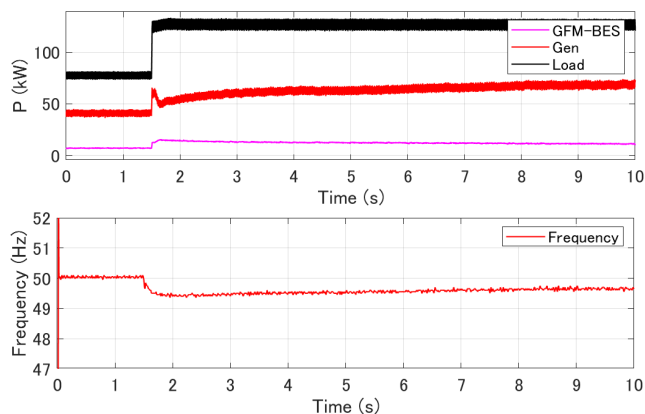

FIGURE 17. Case 6: Power sharing and grid frequency change for zero GFL-BES units, five GFM-BES units, and one SG.
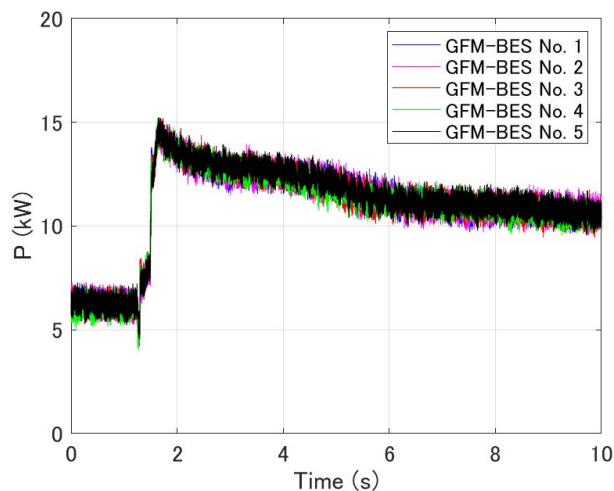

FIGURE 18. Load sharing comparison of each GFM-BES in case 6.

GFM-BES units are connected with a transformer with a rated power of 150 kVA, rated voltage of 440 V, and impedance of 3.71 %, and one GFM-BES unit is connected with a transformer with a rated power of 50 kVA, rated voltage of 440 V, and impedance of 3.28 %. As shown in Figure 18, the

transient and steady-state characteristics of each GFM-BES unit are almost the same, confirming that the influence of different transformer impedance is small.

C. INERTIA EVALUATION VERSUS GFM-BES PENETRATION RATIO

Evaluation of the inertial effect for different GFM-BES penetrations ratio is discussed in this section. Frequency regulation with different GFM-BES penetrations is shown in Figure 19. In the case of one GFM-BES unit, the load fluctuation exceeds the surplus capacity of the GFM-BES, and as shown in Figure 13, the GFM-BES is inactivated by the protection function. Thus, case 2 was excluded from the comparison. It was confirmed that when the load changed, the GFM-BES contributed to frequency adjustment. One index for evaluating the inertia is the minimum frequency nadir. As the penetration ratio of the GFM-BES increases, the frequency nadir increases significantly. Compared with zero and five GFM-BES units, the minimum frequency nadir with respect to load fluctuation could be reduced by 1.75 Hz. The frequency nadir in different cases is summarized in Table 6.
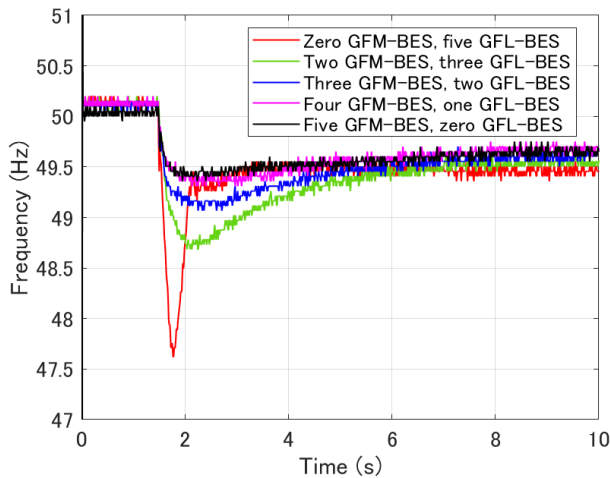

FIGURE 19. Frequency regulation with different penetrations.

TABLE 6. Inertia evaluation.

Metric	Case 1	Case 3	Case 4	Case 5	Case 6
GFM-BES penetration (%)	0	17.7	26.6	35.5	44.4
Frequency nadir (Hz)	47.62	48.68	49.07	49.36	49.37
Maxmium Frequency deviation (Hz)	2.38	1.32	0.93	0.64	0.63
RoCoF (Hz/s)	7.93	2.44	1.52	1.23	1.13
Steady state frequency (Hz)	49.47	49.53	49.61	49.65	49.67

The other evaluation index of inertia is the rate of change of frequency (RoCoF). The RoCoF evaluation index is defined as the frequency reduction rate at the time of system upset as
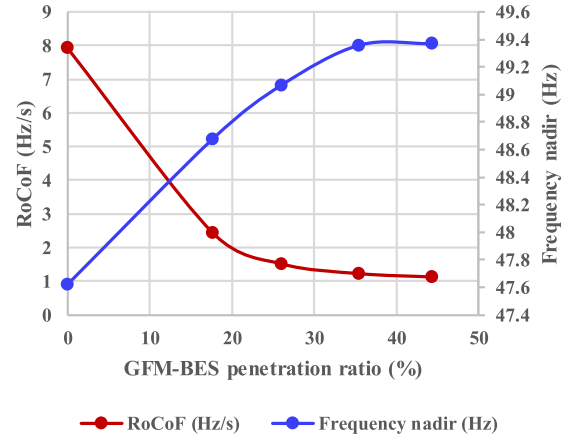

FIGURE 20. RoCoF index and Frequency nadir with different penetrations ratio of GFM-BES.

shown in (10).

$$\text{RoCoF} = \frac{\Delta_f}{\Delta t} \quad (10)$$

The grid code RoCoF limit in English and Ailland is 1 Hz/s (Δt is 0.5 s); in Germany is 2 Hz/s (Δt is 0.5 s); in Spain, Italy and Denmark is 2 Hz/s (Δt is 1 s). However, the gird code RoCoF limit in Japan has not been decided. According to grid interconnection regulations, power generation devices need to be able to tolerate (continue to operate) under a frequency fluctuation of 2 Hz/s (the fault ride-through regulation). In this study, $\Delta t = 0.1$ s is used for the RoCoF calculation by giving consideration to the minimum detection time in this paper. It is assumed that distributed power generation devices follow this regulation. The RoCoF in different cases is summarized in Table 6.

In case 1 and case 3, the RoCoF is over 2 Hz/s. In particular, two GFM-BES units are active in case 3, and when the RoCoF exceeds 2 Hz/s, the distributed power generation devices are consecutively dropped, further reducing the frequency that may lead to a blackout. In case 4, the GFM-BES penetration is 26%, and operation is considered to be stable even when a large load change occurs either on-grid or off-grid. It was confirmed that increasing the GFM-BES penetration can improve the inertia of the power system. The trend of the frequency change rate and frequency nadir due to the different GFM-BES penetrations ratio are compared in Figure 20. It can be found that the RoCoF will lower than 2 Hz/s if the penetration ratio of the GFM-BES is over 20%. The frequency change rate of the generation system is reduced significantly, and the frequency nadir is increased significantly by increasing the GFM-BES penetration, which also verified that system inertia increases with increasing the GFM-BES penetration ratio.

D. POWER SHARING EVALUATION VERSUS GFM-BES PENETRATION RATIO

Load sharing of one GFM-BES unit and an SG with different GFM-BES penetrations is shown in Figures 21 and 22,
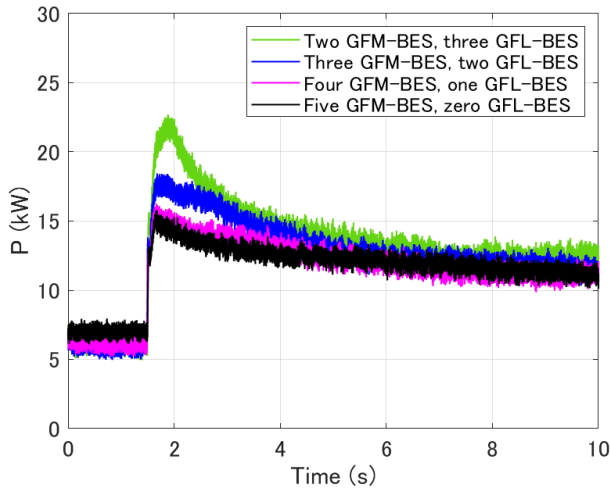
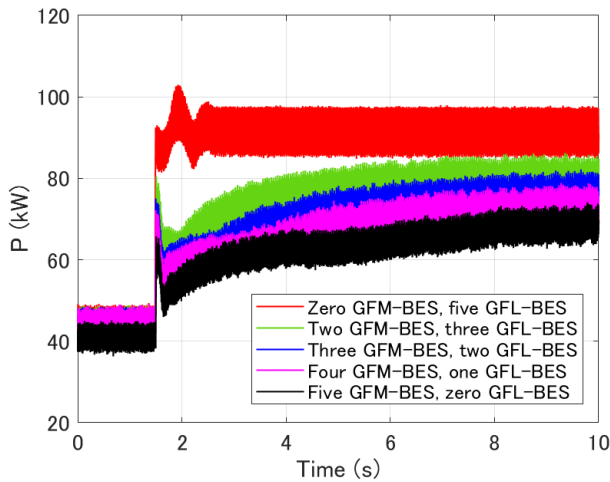**FIGURE 21.** Load sharing of one GFM-BES with different penetrations of GFM-BES.

FIGURE 22. Load sharing of SG with different penetrations of GFM-BES.

TABLE 7. Power sharing evaluation.

Metric	Case 1	Case 3	Case 4	Case 5	Case 6
GFM-BES penetration (%)	0	17.7	26.6	35.5	44.4
Maxmium transient power sharing of SG at t=1.53s (kW)	89.5	76.4	71.9	68	61.6
Maxmium transient power sharing of GFM-BES at t=1.63s (kW)	Not applicable	20.6	17.7	15.8	15.0
Steady state power sharing of SG in calculation (kW)	88	76.3	72.4	69.2	66.6
Steady state power sharing of SG in experiment (kW)	90	83.8	79.8	74.1	69.1
Steady state power sharing of GFM-BES in calculation (kW)	Not applicable	12.2	11.6	11.1	10.6
Steady state power sharing of GFM-BES in experiment (kW)	Not applicable	12.9	12.1	11.8	11.0

respectively. The power sharing in transient and steady states under different GFM-BES penetrations ratio are summarized in Table 7. Steady state load sharing calculated based on (9)
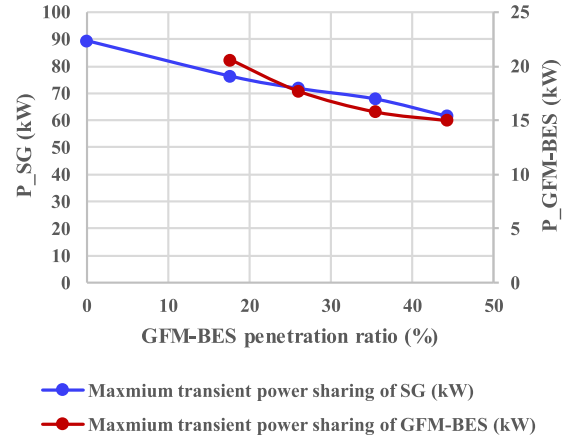

FIGURE 23. Transient load sharing of SG and GFM-BES with different penetrations of GFM-BES.
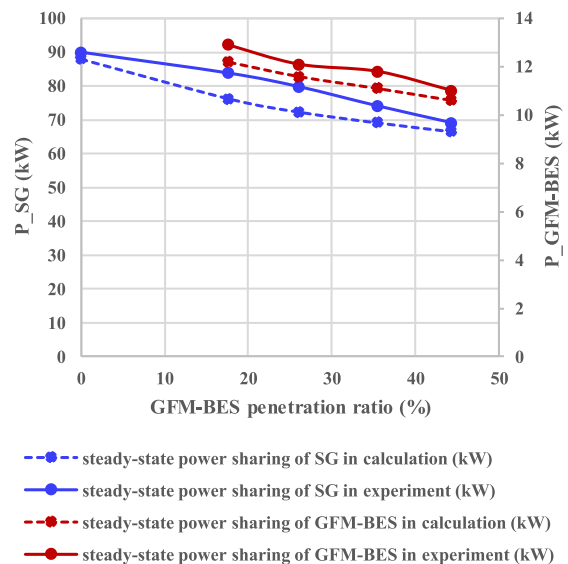

FIGURE 24. Steady state load sharing of SG with different penetrations of GFM-BES.

compared with the experimental results are also summarized in Table 7. Compared with two GFM-BES units in case 3 and five GFM-BES units in case 6, according to the increased system inertia, the maximum transient power sharing of GFM-BES and SG could be reduced by 5.6 kW and 14.8 kW, respectively. According to the GFM-BES droop control, the load sharing of GFM-BES and SG in the steady state could be reduced by 1.9 kW and 14.7 kW, respectively. The trend of the transient load sharing of SG and GFM-BES with different penetrations of GFM-BES are shown in Figure 23. The transient load sharing reduced linearly by increasing the GFM-BES penetration. It can be found that the maximum transient power sharing of GFM-BES is lower than 20 kW if the penetration ratio of the GFM-BES is over 20 %. The GFM-BES will operate in safety because the rated power of GFM-BES is 20 kW. The trend of the steady-state load sharing of GFM-BES and SG with different penetrations of GFM-BES in simulation and experiment are shown in Figure 24. The steady-state load sharing also reduced linearly

by increasing the GFM-BES penetration. The error between the simulation results and the experimental results is less than 10%.

The results confirm that it is possible for multiple GFM-BES units in parallel with diesel SG and GFL-BES to respond automatically to load fluctuations within a few seconds. By increasing the GFM-BES penetration, the system inertia and transient tolerance also improved. The steady-state power sharing effect by the droop control of the GFM-BES was also confirmed.

VI. CONCLUSION

In this study, a large-scale power grid simulating an actual microgrid in Mutsuzawa, Japan was built according to the actual microgrid architecture and simulated with an approximately 1:1 power capacity scale. The grid contains SGs and inverter-BES units. In the simulated grid, the power generation penetration of the inverter-BES units reached 44.4%. Autonomous operation of the simulated grid to achieve frequency regulation was demonstrated without relying on a communication network. Many advanced functions, namely grid forming, synchronization, frequency regulation, and power sharing, were demonstrated through field tests. Improved system inertia and power sharing were demonstrated by increasing the penetration of GFM-BES units for different cases. The inertia constant of a diesel SG was inferred from simulations and experiments to be approximately 1.12 s, which is very small. An unexpected problem also occurred, during the step load change experiment, in which the GFM-BES shut down when the GFM-BES penetration ratio was low because of the low inertia of the SG.

In the microgird of this study, the penetration ratio of the GFM-BES needs larger than 20 % to meet the RoCoF standard for system stability.

The field trial demonstrated that the GFM-BES improved grid stability, reliability, security, and resiliency without relying on communication networks. In the future, if the proportion of renewable energy power sources increases, it should be possible to compensate for the decrease in inertial force by using the GFM-BES technology. This project is expected to demonstrate a new lifestyle, with natural sustainable resources for improved resiliency.

REFERENCES

[1] S. Golestan, J. M. Guerrero, and J. C. Vasquez, "Three-phase PLLs: A review of recent advances," *IEEE Trans. Power Electron.*, vol. 32, no. 3, pp. 1894–1907, Mar. 2017, doi: 10.1109/TPEL.2016.2565642.

[2] Y. Lin, J. Eto, B. Johnson, J. Flicker, R. Lasseter, H. Pico, G. Seo, B. Pierre, and A. Ellis, "Research roadmap on grid-forming inverters," NREL, Golden, CO, USA, Tech. Rep. NREL/TP-5D00-73476, 2020.

[3] M. C. Chandorkar, D. M. Divan, and R. Adapa, "Control of parallel connected inverters in standalone AC supply systems," *IEEE Trans. Ind. Appl.*, vol. 29, no. 1, pp. 136–143, Jan./Feb. 1993, doi: 10.1109/28.195899.

[4] K. De Brabandere, B. Bolsens, J. Van den Keybus, A. Woyte, J. Driesen, and R. Belmans, "A voltage and frequency droop control method for parallel inverters," *IEEE Trans. Power Electron.*, vol. 22, no. 4, pp. 1107–1115, Jul. 2007, doi: 10.1109/TPEL.2007.900456.

[5] H. Nikkhajoei and R. H. Lasseter, "Distributed generation interface to the CERTS microgrid," *IEEE Trans. Power Del.*, vol. 24, no. 3, pp. 1598–1608, Jul. 2009, doi: 10.1109/TPWRD.2009.2021040.

[6] J. M. Guerrero, J. C. Vasquez, J. Matas, L. G. de Vicuna, and M. Castilla, "Hierarchical control of droop-controlled AC and DC microgrids—A general approach toward standardization," *IEEE Trans. Ind. Electron.*, vol. 58, no. 1, pp. 158–172, Jan. 2011, doi: 10.1109/TIE.2010.2066534.

[7] H.-P. Beck and R. Hesse, "Virtual synchronous machine," in *Proc. 9th Int. Conf. Electr. Power Quality Utilisation*, Barcelona, Spain, Oct. 2007, p. 6.

[8] K. Visscher and S. W. H. De Haan, "Virtual synchronous machines (VSG'S) for frequency stabilisation in future grids with a significant share of decentralized generation," in *Proc. CIRED Seminar, SmartGrids Distrib.*, 2008, pp. 1–4.

[9] Y. Chen, R. Hesse, D. Turschner, and H.-P. Beck, "Improving the grid power quality using virtual synchronous machines," in *Proc. Int. Conf. Power Eng., Energy Electr. Drives*, May 2011, pp. 1–6.

[10] Y. Chen, R. Hesse, D. Turschner, and H.-P. Beck, "Investigation of the virtual synchronous machine in the island mode," in *Proc. 3rd IEEE PES Innov. Smart Grid Technol. Eur. (ISGT Europe)*, Oct. 2012, pp. 1–6.

[11] Q.-C. Zhong and G. Weiss, "Synchronverters: Inverters that mimic synchronous generators," *IEEE Trans. Ind. Electron.*, vol. 58, no. 4, pp. 1259–1267, Apr. 2011, doi: 10.1109/TIE.2010.2048839.

[12] Q.-C. Zhong, "Virtual synchronous machines: A unified interface for grid integration," *IEEE Power Electron. Mag.*, vol. 3, no. 4, pp. 18–27, Dec. 2016, doi: 10.1109/MPEL.2016.2614906.

[13] Q.-C. Zhong, W.-L. Ming, and Y. Zeng, "Self-synchronized universal droop controller," *IEEE Access*, vol. 4, pp. 7145–7153, 2016, doi: 10.1109/ACCESS.2016.2616115.

[14] Q.-C. Zhong, Y. Wang, and B. Ren, "Connecting the home grid to the public grid: Field demonstration of virtual synchronous machines," *IEEE Power Electron. Mag.*, vol. 6, no. 4, pp. 41–49, Dec. 2019, doi: 10.1109/MPEL.2019.2946700.

[15] H. Alatrash, A. Mensah, E. Mark, G. Haddad, and J. Enslin, "Generator emulation controls for photovoltaic inverters," *IEEE Trans. Smart Grid*, vol. 3, no. 2, pp. 996–1011, Jun. 2012, doi: 10.1109/TSG.2012.2188916.

[16] M. Rahmani, Y. Herriot, C. Guyon-Aubert, D. Gualino, A. Dentella, S. Lechat-Sanjuan, and G. Gandanegara, "Control method of a virtual generator," U.S. Patent 2017 0 235 322, Aug. 17, 2017.

[17] K. Sakimoto, Y. Miura, and T. Ise, "Stabilization of a power system with a distributed generator by a virtual synchronous generator function," in *Proc. 8th Int. Conf. Power Electron.-ECCE Asia*, May 2011, pp. 1498–1505.

[18] H. Bevrani, T. Ise, and Y. Miura, "Virtual synchronous generators: A survey and new perspectives," *Int. J. Electr. Power Energy Syst.*, vol. 54, pp. 244–254, Jan. 2014, 0142-0615, doi: 10.1016/IJEPES.2013.07009.

[19] F. Mandrile, E. Carpaneto, E. Armando, and R. Bojoi, "Simple tuning method of virtual synchronous generators reactive control," in *Proc. IEEE Energy Convers. Congr. Expo. (ECCE)*, Oct. 2020, pp. 2779–2785.

[20] H. Xu, X. Zhang, F. Liu, R. Shi, C. Yu, and R. Cao, "A reactive power sharing strategy of VSG based on virtual capacitor algorithm," *IEEE Trans. Ind. Electron.*, vol. 64, no. 9, pp. 7520–7531, Sep. 2017, doi: 10.1109/TIE.2017.2686374.

[21] Y. Noro, "Proposal of inverter control method for electric power system consisting of energy storages," *IEEJ Trans. PE*, vol. 138, no. 11, pp. 854–861, 2018, doi: 10.1541/IEEJPES.2018.138864.

[22] Y. Ma, F. Wang, and L. M. Tolbert, "Virtual synchronous generator with limited current—Impact on system transient stability and its mitigation," in *Proc. IEEE Energy Convers. Congr. Expo. (ECCE)*, Oct. 2020, pp. 2773–2778.

[23] Q.-C. Zhong and G. C. Konstantopoulos, "Current-limiting droop control of grid-connected inverters," *IEEE Trans. Ind. Electron.*, vol. 64, no. 7, pp. 5963–5973, Jul. 2017, doi: 10.1109/TIE.2016.2622402.

[24] I. Sadeghkhani, M. E. H. Golshan, J. M. Guerrero, and A. Mehrizi-Sani, "A current limiting strategy to improve fault ride-through of inverter interfaced autonomous microgrids," *IEEE Trans. Smart Grid*, vol. 8, no. 5, pp. 2138–2148, Sep. 2017, doi: 10.1109/TSG.2016.2517201.

[25] K. Shi, W. Song, P. Xu, Z. Fang, and Y. Ji, "Low-voltage ride-through control strategy for a virtual synchronous generator based on smooth switching," *IEEE Access*, vol. 6, pp. 2703–2711, 2018, doi: 10.1109/ACCESS.2017.2784846.

[26] R. Zeng and M. S. Chinthavali, "Fault ride-through control strategy for single-phase virtual synchronous generator," in *Proc. IEEE Power Energy Soc. Innov. Smart Grid Technol. Conf. (ISGT)*, Feb. 2019, pp. 1–5.

[27] J. Liu, Y. Miura, and T. Ise, "Comparison of dynamic characteristics between virtual synchronous generator and droop control in inverter-based distributed generators," *IEEE Trans. Power Electron.*, vol. 31, no. 5, pp. 3600–3611, May 2016, doi: 10.1109/TPEL.2015.2465852.

[28] J. Liu, Y. Miura, H. Bevrani, and T. Ise, "A unified modeling method of virtual synchronous generator for multi-operation-mode analyses," *IEEE J. Emerg. Sel. Topics Power Electron.*, vol. 9, no. 2, pp. 2394–2409, Apr. 2021, doi: 10.1109/JESTPE.2020.2970025.

[29] K. Sakimoto, Y. Miura, and T. Ise, "Stabilization of a power system including inverter type distributed generators by the virtual synchronous generator," *IEEJ Trans. Power Energy*, vol. 132, no. 4, pp. 341–349, Apr. 2012, doi: 10.1541/IEEJPES.2012.132341.

[30] H. S. Hlaing, J. Liu, Y. Miura, H. Bevrani, and T. Ise, "Enhanced performance of a stand-alone gas-engine generator using virtual synchronous generator and energy storage system," *IEEE Access*, vol. 7, pp. 176960–176970, 2019, doi: 10.1109/ACCESS.2019.2957890.

[31] B. B. Johnson, S. V. Dhople, A. O. Hamadeh, and P. T. Krein, "Synchronization of parallel single-phase inverters with virtual oscillator control," *IEEE Trans. Power Electron.*, vol. 29, no. 11, pp. 6124–6138, Nov. 2014, doi: 10.1109/TPEL.2013.2296292.

QIANG LIN (Member, IEEE) received the M.Eng. degree in electrical and electronics engineering from Kyushu University, Fukuoka, Japan, in 2017. He has been a Researcher with the Toshiba Corporate Research and Development Center, since 2020. His current research interests include micro-grid control, power electronics, and electromagnetic interference/electromagnetic compatibility. He received the Young Engineers Award of the Institute of Electronics, Information and Communication Engineers (IEICE), Japan, in 2019, and the Young Engineers Presentation Competition Award of Institute of Electrical Engineers of Japan, in 2021.

HIROSHI UNO received the M.Eng. degree in mathematical, electronic, and information systems from the Graduate School of Science and Engineering, Saitama University, in March 2019. He joined Toshiba Corporation, in April 2019. His current research interests include wireless charging system and micro-grid. He is a member of the Institute of Electrical Engineers of Japan.

KENICHIRO OGAWA received the M.Eng. degree from the Department of Applied Science for Electronics and Materials, Kyushu University, in March 2009. He joined Toshiba Corporation, in April 2009. His current research interest includes wireless charging systems.

YASUHIRO KANEKIYO joined Toshiba Corporation, in April 1985. He is engaged in the development of microwave and high frequency circuits and subsystem products at the company's Komukai Factory. Currently, he is with the Research and Development Center of the company engaged in research on wireless power transmission systems.

TETSU SHIJO (Member, IEEE) received the B.S., M.S., and D.E. degrees in electrical and electronic engineering from the Tokyo Institute of Technology, Tokyo, Japan, in 2002, 2004, and 2007, respectively. He was a Research Fellow of the Japan Society for the Promotion of Science, from 2004 to 2007. He has been with the Toshiba Corporate Research and Development Center, since 2007. He received the Young Engineers Award of the Institute of Electronics, Information and Communication Engineers (IEICE), Japan, in 2004, and the TELECOM Social Science Award for Students, in 2005.

JUNICHI ARAI (Life Senior Member, IEEE) received the B.S. degree and M.S. degree in electrical engineering from Waseda University, in 1970 and 1972, respectively, and the Ph.D. degree in engineering from Tokyo Metropolitan University, Japan, in 1995. He joined as a Research Engineer of power systems at Toshiba Corporation, in 1972. He has been a Professor with the Engineering Department, Kogakuin University, Tokyo, since 2006, where he is currently a Professor Emeritus and an Executive Researcher with the Energy and Environment Technology Research Institute. His research interests include power system control, power electronics applications, micro-grid control, and power quality. He is a fellow of IET, C.Eng, and IEEJ.

TAKESHI MATSUDA received the M.Eng. and Ph.D. degrees from the Department of Urban Environmental Studies, Kyoto University, in 2011 and 2015, respectively. He joined Pacific Consultants Company Ltd., in 2011. He has been with Pacific Power Company Ltd., since 2015, where he is currently a Deputy General Manager with the Planning Department and the General Manager of VPP Business Office. He is mainly engaged in project management of regional energy business and virtual power plant business centered on local government new electric power.

DAIKI YAMASHITA received the Ph.D. degree from the Graduate School of Environment and Energy, Waseda University. He was a Lecturer at the Faculty of Science and Technology, Waseda University, from 2014 to 2016. He joined Pacific Consultants Company Ltd., in 2016, where he is currently an Assistant Manager with the Environment and Energy Department, Social Innovation Business Headquarters, and an Invited Researcher with the Institute for Next-Generation Science and Technology Economic Analysis, Waseda University. He is mainly engaged in the planning and design of micro-grid energy systems. He was a fellow of the Japan Society for the Promotion of Science (JSPS), from 2012 to 2014.

KENJI OTANI received the master's degree from the Graduate School of Engineering, Tokyo University of Agriculture and Technology, in 1995. In 1995, he joined the National Institute of Advanced Industrial Science and Technology, where he has been the Research Team Leader of the Renewable Energy Research Center Energy Network Team, since 2014. He is engaged in the operation analysis and optimal design research of photovoltaic power generation systems.

• • •